Supplementary Information

Zinc-Induced Polycrystalline Transformation of High-Entropy Fluorides and Derived Regulatory Mechanisms on Bifunctional Oxygen Electrocatalysis

Gang Wang[a], Hao Chi[a], Yang Feng[b], Jie Fan[a], Nanping Deng[a,*], Weimin Kang[a,*], Bowen Cheng[c,*].

[a] *State Key Laboratory of Separation Membranes and Membrane Processes, School of Textile Science and Engineering, Tiangong University, Tianjin, 300387, PR China*

[b] *State Key Laboratory of Advanced Chemical Power Sources, College of Chemistry, Nankai University, Tianjin 300071, PR China*

[c] *School of Material Science and Engineering, Tiangong University, Tianjin 300387, PR China*

* Corresponding author. E-mail addresses: dengnanping@tiangong.edu.cn (N. P. Deng), kangweimin@tiangong.edu.cn (W. M. Kang), bowen15@tiangong.edu.cn (B. W. Cheng)

The calculation method of configurational entropy for fluorides:

For high-entropy materials (HEM), a high mixing entropy (ΔS_{mix}) can greatly reduce the system's free energy, ultimately leading to a system with excellent stability[1]. Specifically, the entropies of the system mainly includes configurational entropy (ΔS_{conf}), vibrational entropy (ΔS_{vib}), magnetic dipole entropy (ΔS_{mag}) and electronic randomness entropy (ΔS_{elec}). Generally, configurational entropy plays a dominant role[2]. The concept of entropy stabilization is also applicable to multi-component compounds, and high-entropy compounds (including high-entropy fluorides) have begun to be gradually developed[3]. The configurational entropy of high-entropy compounds can be obtained according to the following related equations[4]:

$$\Delta S_{mix} = \Delta S_{conf} + \Delta S_{vib} + \Delta S_{mag} + \Delta S_{elec} \#(S1)$$

$$\Delta S_{mix} \approx \Delta S_{conf} \#(S2)$$

$$\Delta S_{conf} = -R\left[\left(\sum_{i=1}^{n} x_i \ln x_i\right)_{cation\text{-}site} + \left(\sum_{j=1}^{m} x_j \ln x_j\right)_{anion\text{-}site}\right] \#(S3)$$

where R is the molar gas constant, x_i and x_j represent the molar fractions of elements in the cation and anion sites, respectively.

Electrochemical measurement parameters:

All electrochemical tests of the three-electrode system with independent variables noted as "Potential (V vs. RHE)" are independent of each other. The ink should be fully shaken and continuously ultrasonicated for more than 30 minutes before the dispensing process. It should be dispensed within 10 minutes, and then the prepared electrode should be placed in a cool place to fully dry for 1 hour. Corresponding electrochemical tests have been conducted for 50 pre-cycles. The pre-cycle is scanned from 0 V to 1.2 V (vs. RHE) by cyclic voltammetry with a sweep rate of 100 mV s^{-1}. The ORR-LSV process is scanned from 1.1 V to 0.1 V (vs. RHE) by the GC rotating disk electrode covered

with 0.2 mg cm^{-2} catalyst with a scan rate of 10 mV s^{-1} in O_2 saturated 0.1 M KOH. The corresponding Tafel slope can be obtained from the LSV data. The potential of the Pt ring electrode in RRDE is fixed at 1.2 V (vs. RHE), and 50 cycles of pre-cycle scans of 0 V to 1.2 V (vs. RHE) are performed before the test. The fixed potential is 0.7 V (vs. RHE) for ORR long-term stability tests. The OER-LSV process scans from 1.1 V to 1.8 V (vs. RHE) through Ni-foam (untreated) covered with 0.5 mg cm^{-2} catalyst at a sweep rate of 10 mV s^{-1} in O_2 saturated 1.0 M KOH. The corresponding Tafel slope is given by LSV data is obtained. The EIS process scans from high frequency 1000000 Hz to 0.1 Hz. The ZABs test process uses a two-electrode system for measurement in air atmosphere (~21% O_2). The Zn sheet is used as the auxiliary electrode and the reference electrode at the same time, and the hydrophobic carbon paper coated with 1 g cm^{-2} catalyst is used as the working electrode. The power density curve is measured by linear voltammetry, sweeping from 1.5 V to 0.3 V, with a sweep speed of 20 mV s^{-1}. The charge-discharge cycle stability test consists of 10 min of discharge and 10 min of charge, and the current density is 10 mA. cm^{-2}.

Calculation of electrochemical active surface area (ECSA):

As the double layer capacitance (C_{dl}) is proportional to the ECSA and determined from the corresponding cyclic voltammetry (CV) curves. The CV curves was test with the potential range of 0.1 ~ 0.18 V (vs. HgO|Hg) at various scan rates of 10, 20, 30, 40, 50, 60, 70 mV s^{-1}. Then, the current density obtained from the CV curves at each scan rate was calculated by the formula $\Delta j = j_1 - j_2$. $\Delta j/2$ at each scan rate was then linearly fitted by the least-squares method, and the slope value of the curve obtained was C_{dl}. In addition, catalysts that usually have a real surface area of 1 cm^{-2} generally have a specific capacitance value (C_s) in the range of 20 ~ 60 F cm^{-2}, and we took Cs = 40 F cm^{-2}[5, 6]. and then the final ECSA value is calculated by ECSA = C_{dl}/C_s.

Calculation of specific activity:

The specific activities of catalysts for the OER can be evaluated via normalizing the measured kinetic current by ECSA[5].

Table S1. The melting point and boiling point of materials[7]

Elements	Fluoride melting point [°C]	Fluoride boiling point [°C]	Metal melting point [°C]	Metal boiling point [°C]
Mn	930	1820	1244	2095
Co	1127	1400	1494	2927
Ni	1450	1740	1453	2884
Cu	836	1676	1085	2562
Zn	872	1500	420	907

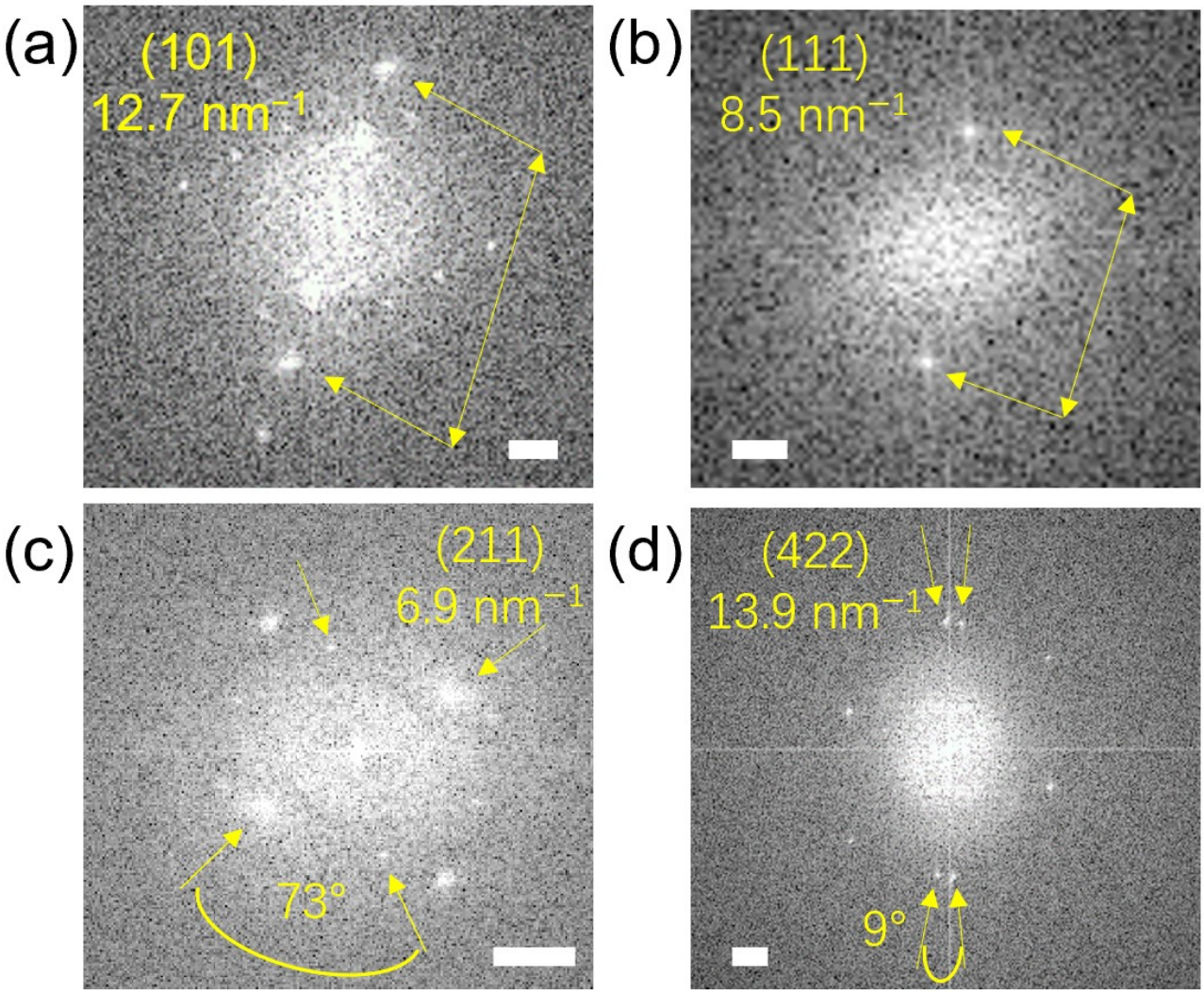

Fig. S1. The selected Area Electron Diffraction (SAED) corresponding to the selected area in **Fig. 2**. (a) (MnNiCu)F_2-PCNFs, (b) (MnNiCuCo)F_2-PCNFs, (c) (MnNiCuZn)F_2-PCNFs, (d) (MnNiCuCoZn)F_2-PCNFs.

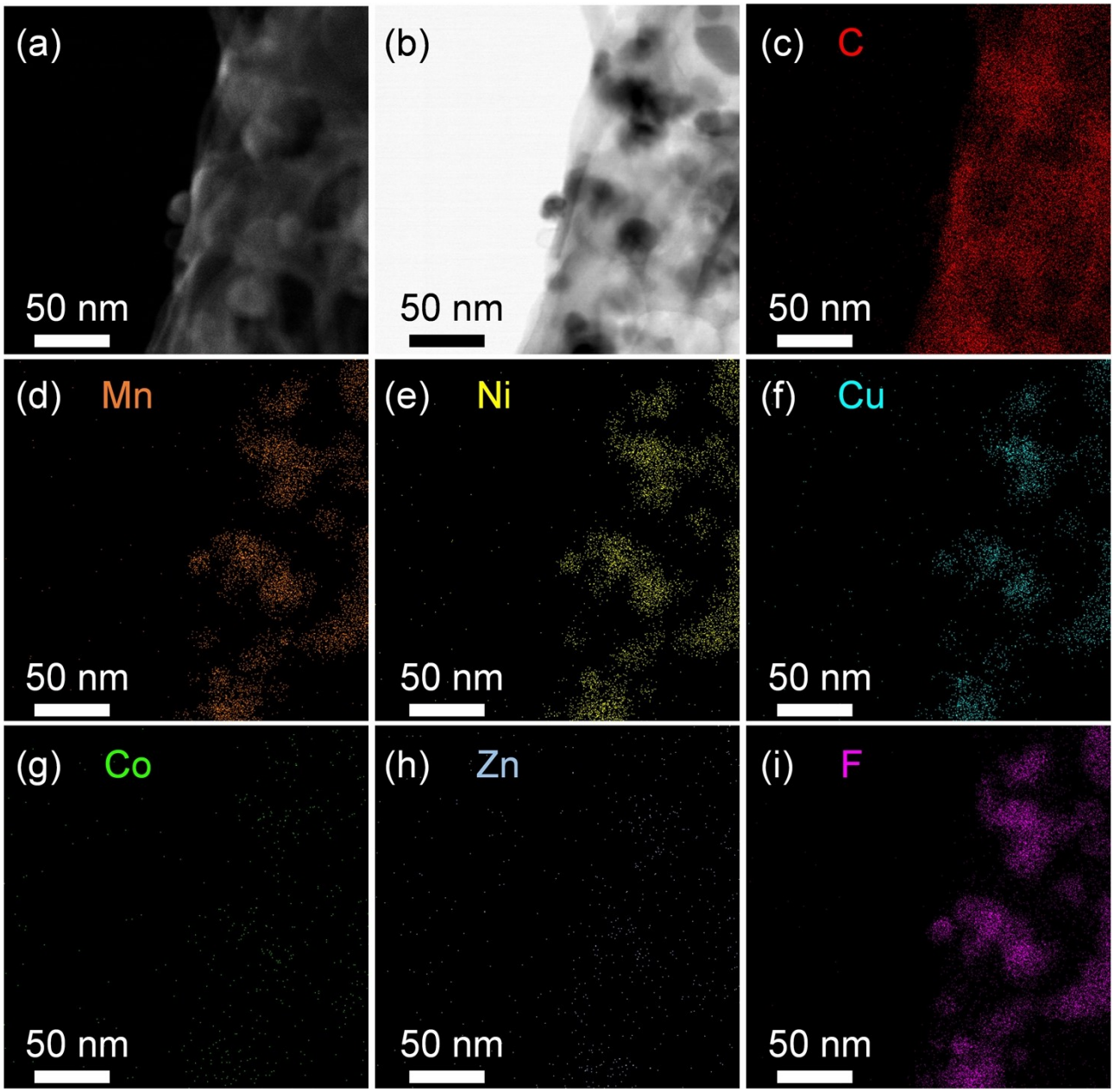

Fig. S2. The **(a, b)** STEM and **(c-i)** corresponding EDS surface scans of (MnNiCu)F_2-PCNFs.

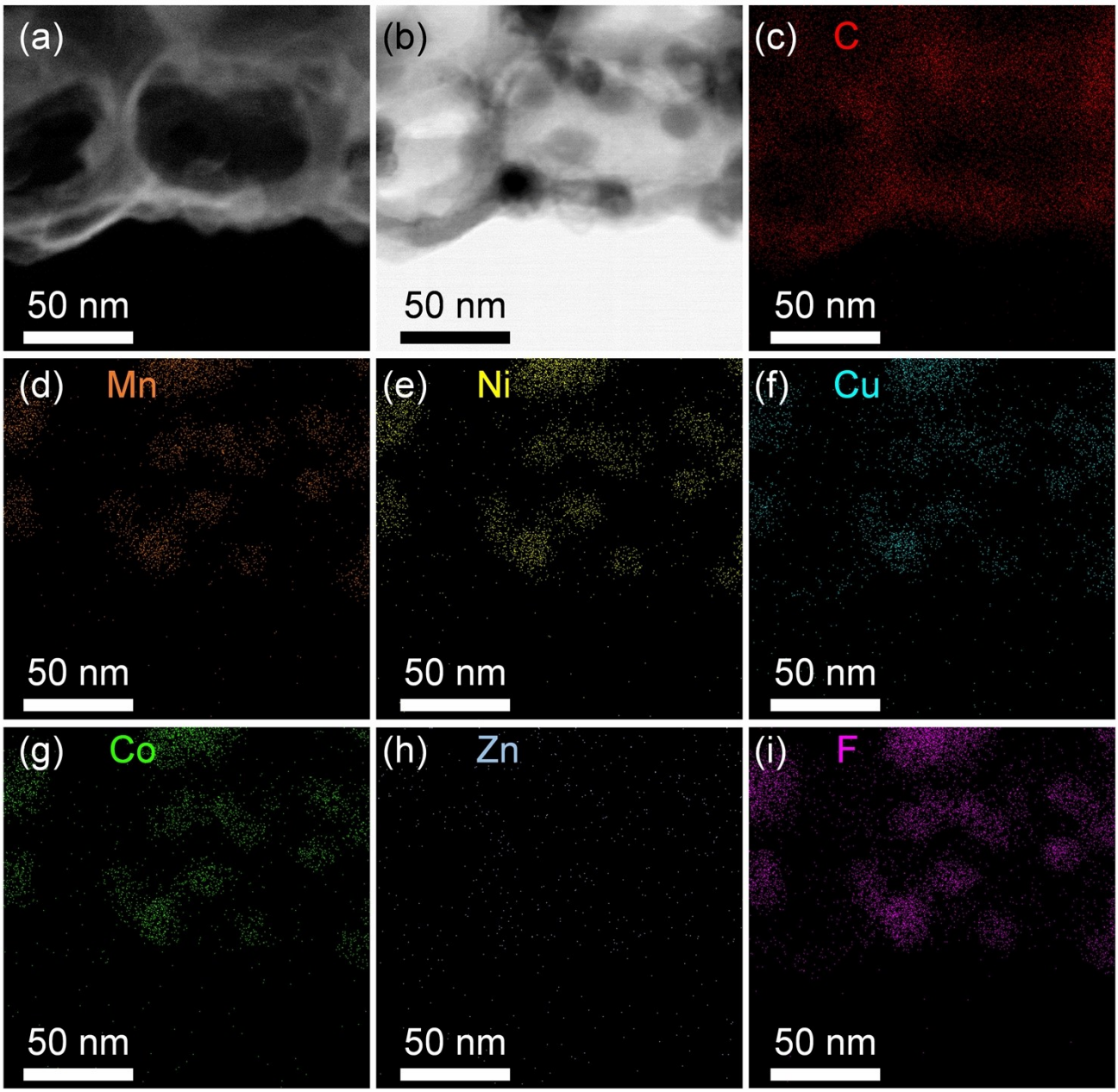

Fig. S3. The **(a, b)** STEM and **(c-i)** corresponding EDS surface scans of (MnNiCuCo)F_2-PCNFs.

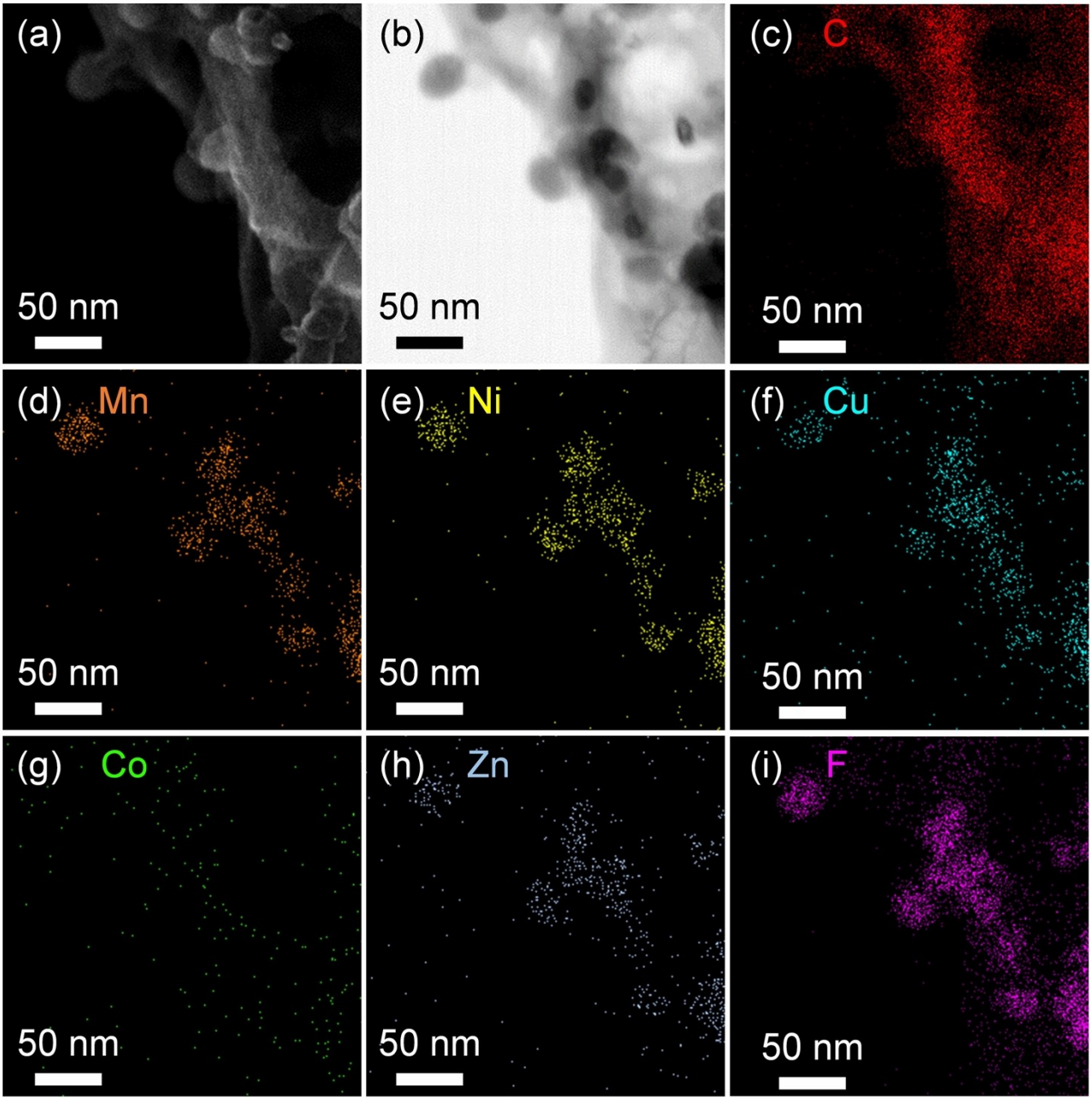

Fig. S4. The **(a, b)** STEM and **(c-i)** corresponding EDS surface scans of (MnNiCuZn)F_2-PCNFs.

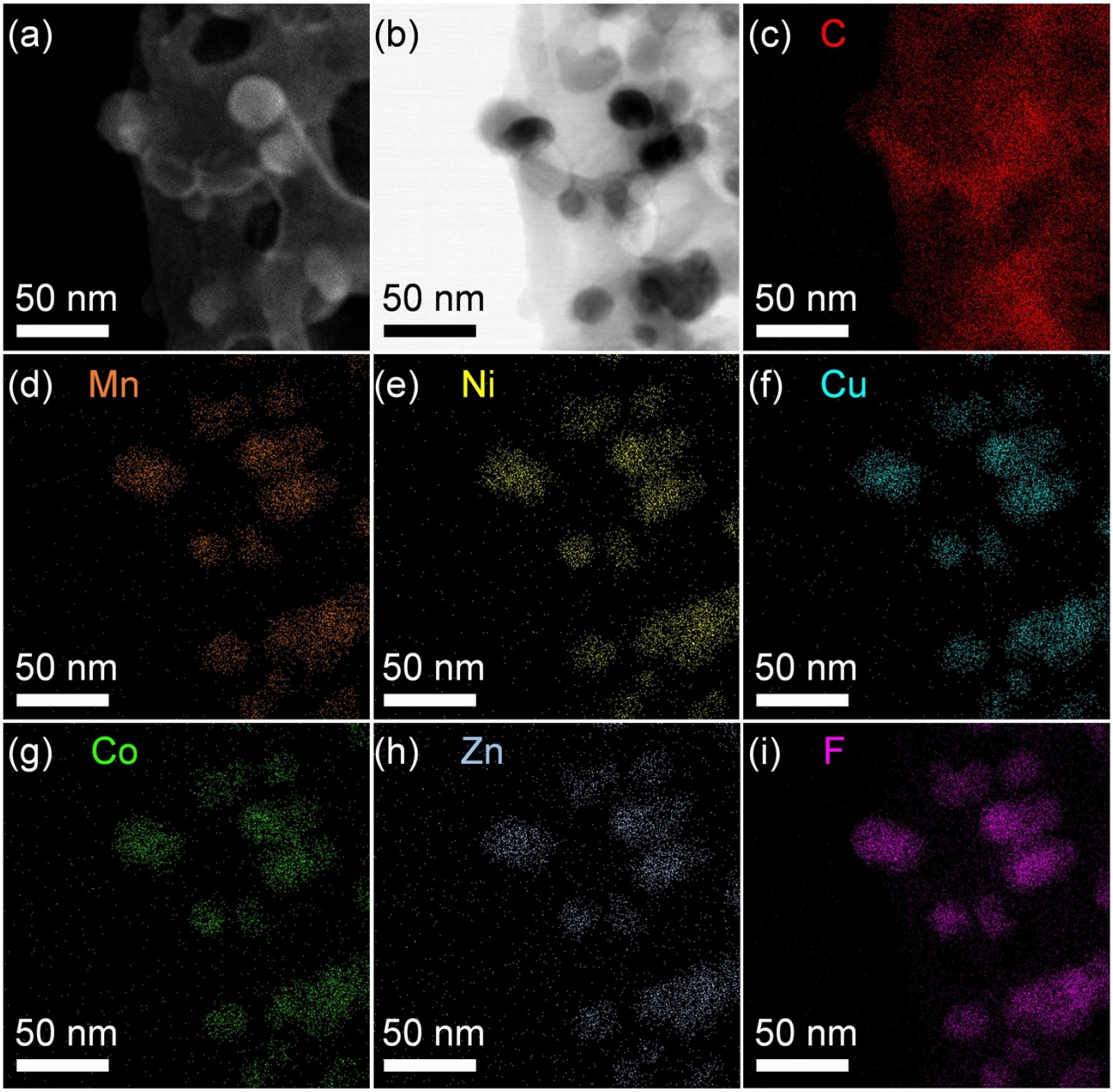

Fig. S5. The **(a, b)** STEM and **(c-i)** corresponding EDS surface scans of (MnNiCuCoZn)F_2-PCNFs.

Table S2. Elemental composition of each sample

Element	$(MnNiCu)F_2$-PCNFs [Atomic %]	$(MnNiCuCo)F_2$-PCNFs [Atomic %]	$(MnNiCuZn)F_2$-PCNFs [Atomic %]	$(MnNiCuCoZn)F_2$-PCNFs [Atomic %]
C	90.93	90.38	92.46	91.05
F	6.61	5.46	5.85	6.39
Mn	0.91	1.07	0.56	0.64
Co	-	1.01	-	0.48
Ni	0.83	1.09	0.42	0.54
Cu	0.72	0.98	0.42	0.52
Zn	-	-	0.27	0.38

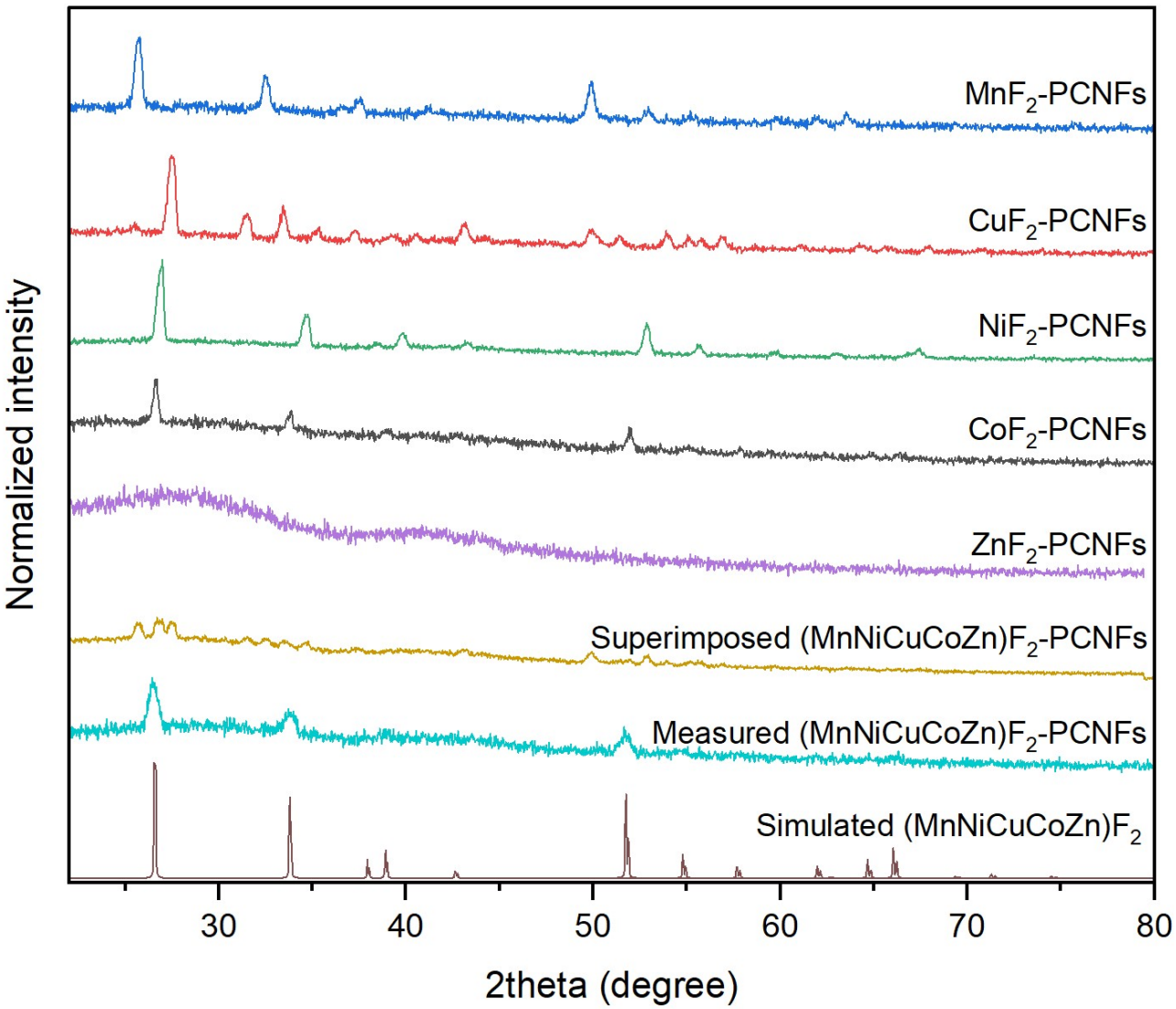

Fig. S6. Individually prepared single-metal fluoride composite PCNFs, superimposed XRD spectra, measured $(MnNiCuCoZn)F_2$-PCNFs and simulated $(MnNiCuCoZn)F_2$.

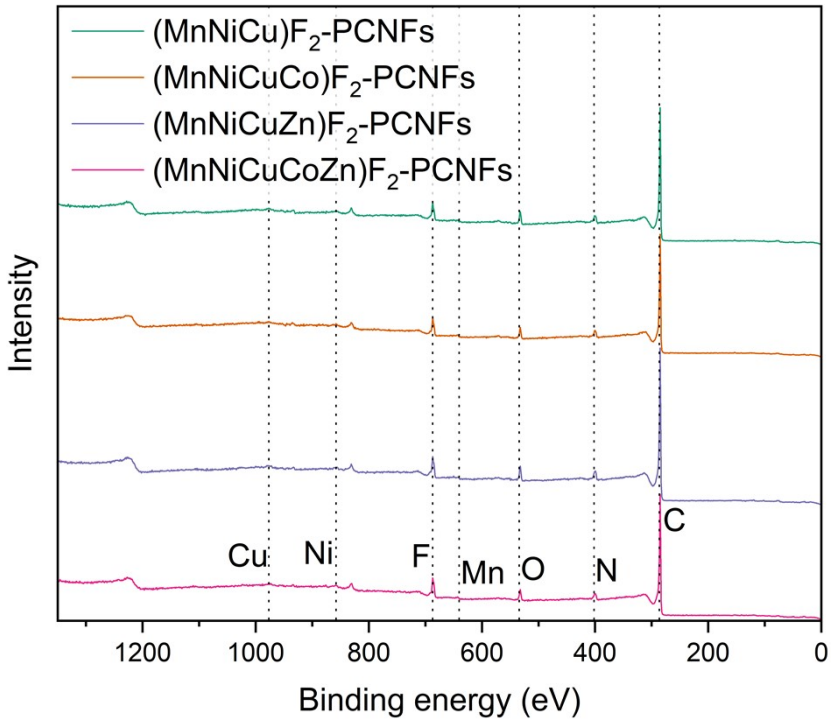

Fig. S7. The XPS spectra of $(MnNiCu)F_2$-PCNFs, $(MnNiCuCo)F_2$-PCNFs, $(MnNiCuZn)F_2$-PCNFs, and $(MnNiCuCoZn)F_2$-PCNFs

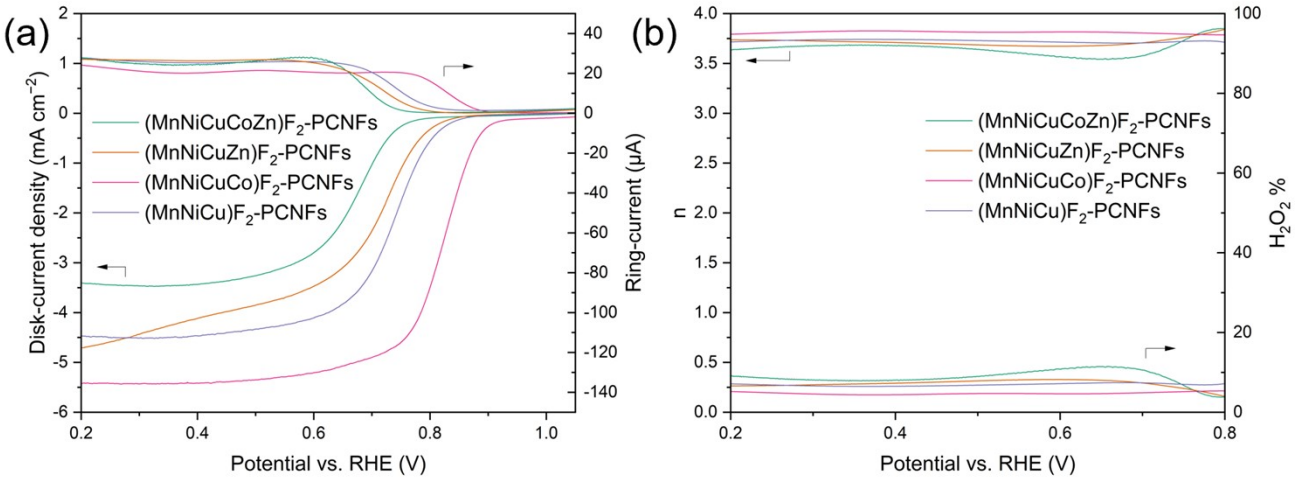

Fig. S8. (**a**) RRDE test, (**b**) corresponding electron transfer number and H_2O_2 yield calculation.

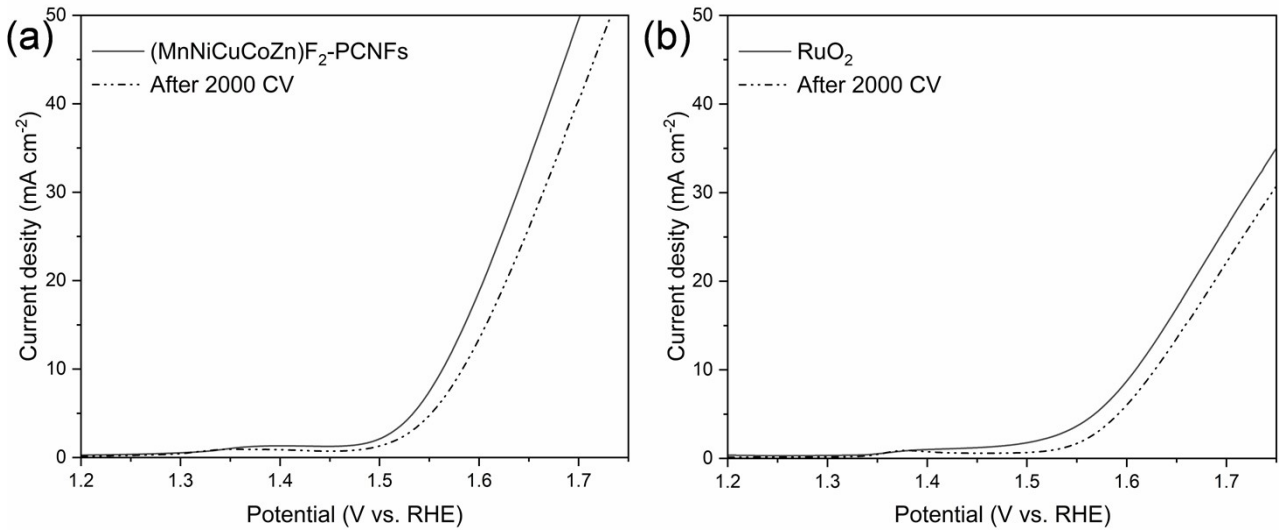

Fig. S9. The corresponding accelerated durability test (ADT) of OER.

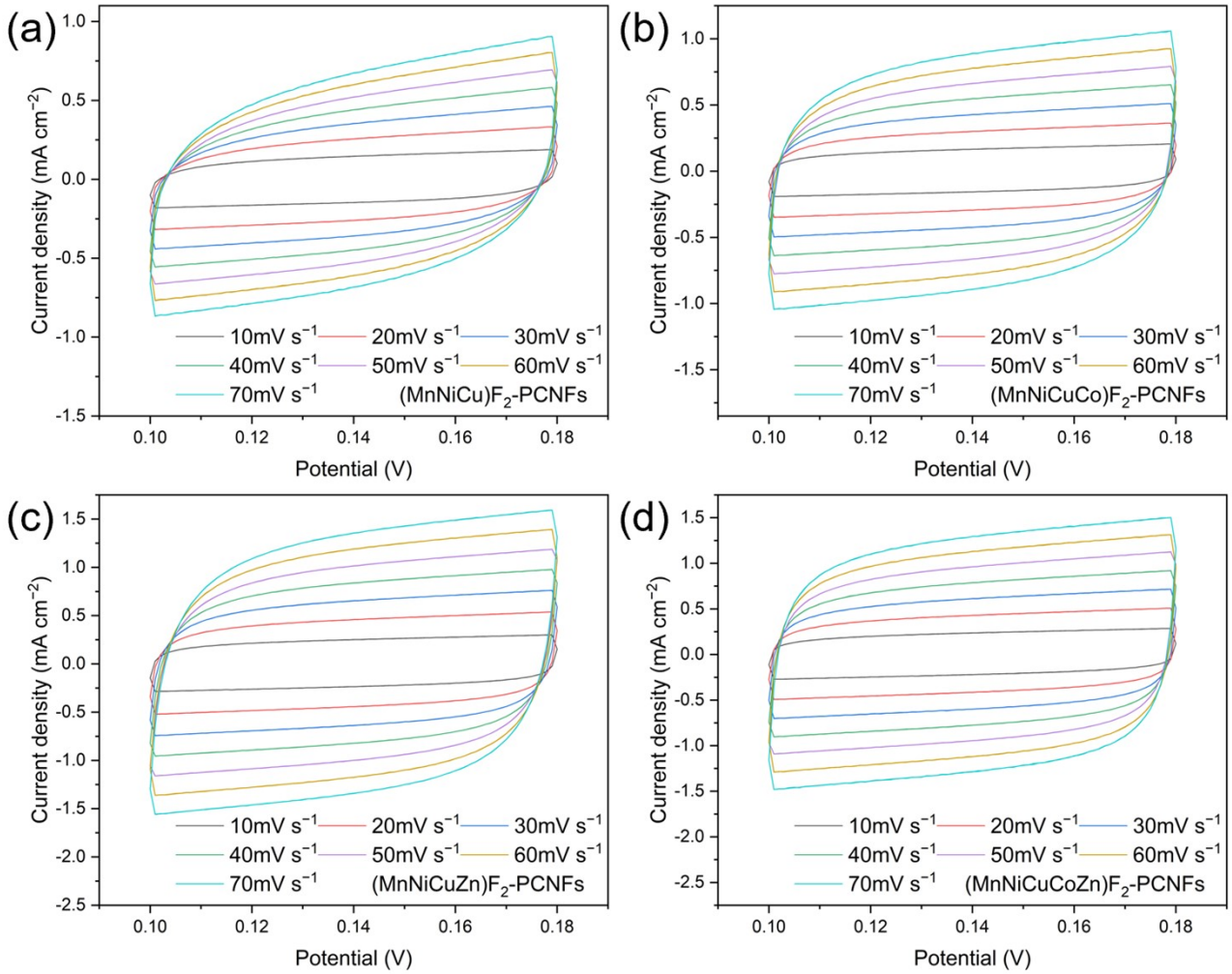

Fig. S10. CV curves of **(a)** (MnNiCu)F_2-PCNFs, **(b)** (MnNiCuCo)F_2-PCNFs, **(c)** (MnNiCuZn)F_2-PCNFs, and **(d)** (MnNiCuCoZn)F_2-PCNFs at different scan rates within the non-Faradaic current range.

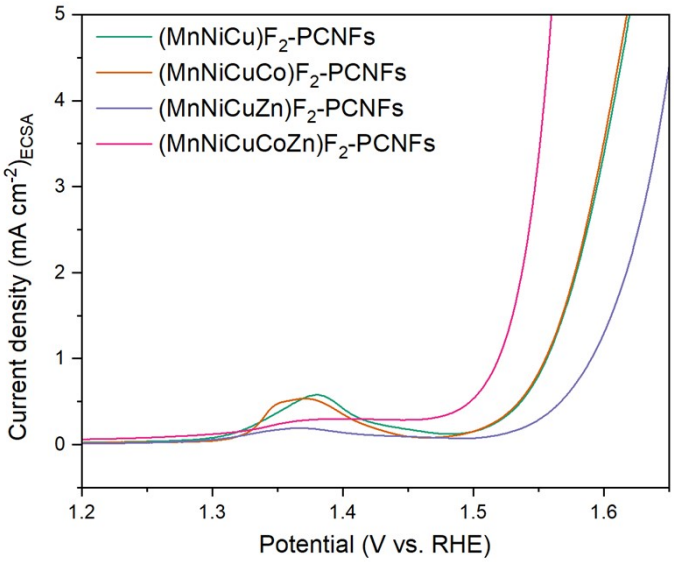

Fig. S11. ECSA-normalized activity of (MnNiCu)F_2-PCNFs, (MnNiCuCo)F_2-PCNFs, (MnNiCuZn)F_2-PCNFs, and (MnNiCuCoZn)F_2-PCNFs

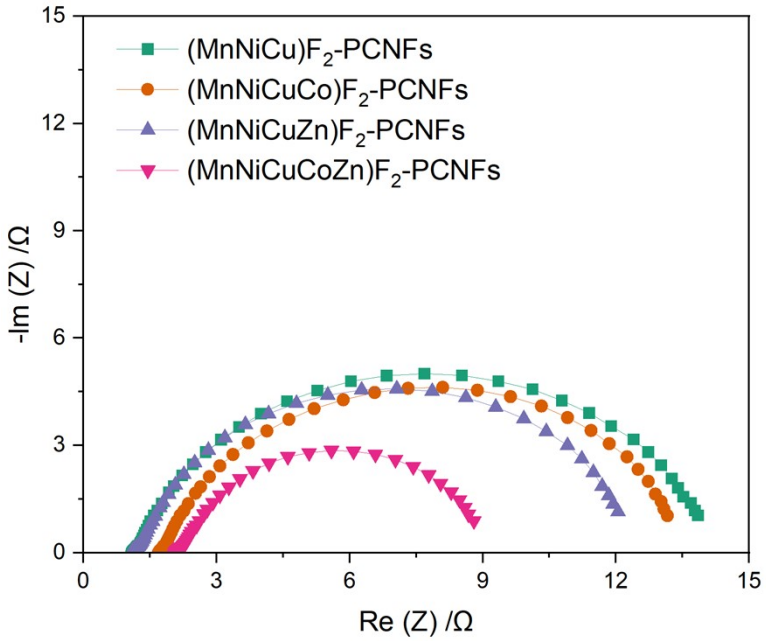

Fig. S12. Nyquist plots of $(MnNiCu)F_2$-PCNFs、$(MnNiCuCo)F_2$-PCNFs、$(MnNiCuZn)F_2$-PCNFs and $(MnNiCuCoZn)F_2$-PCNFs.

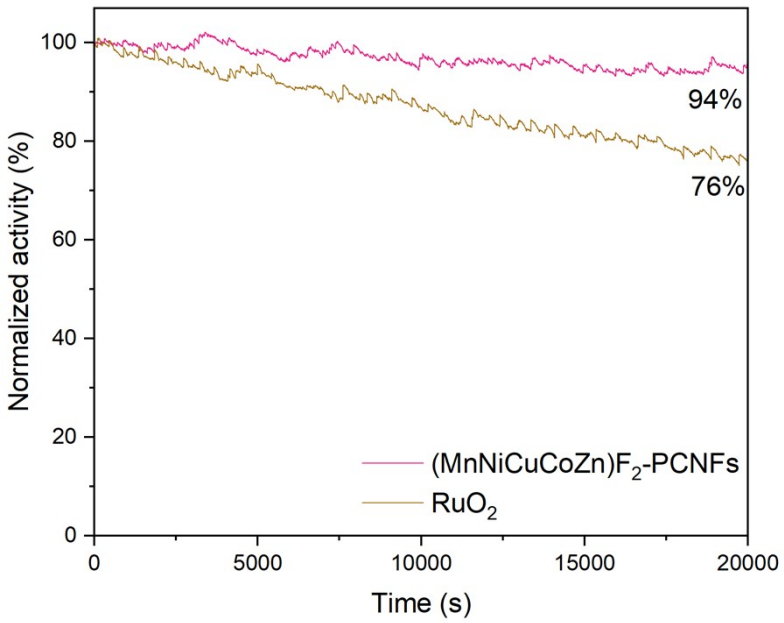

Fig. S13. Long-term stability for OER.

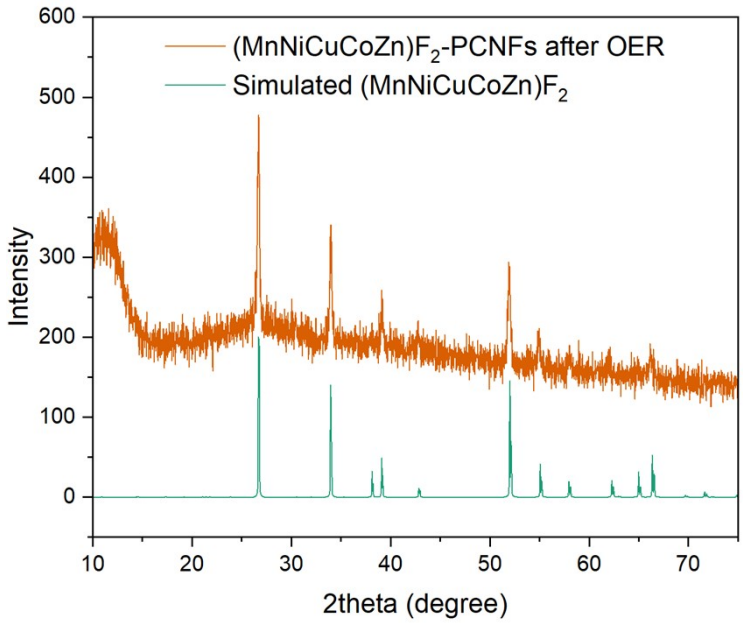

Fig. S14. The XRD spectra of (MnNiCuCoZn)F_2-PCNFs after 20000 s OER process.

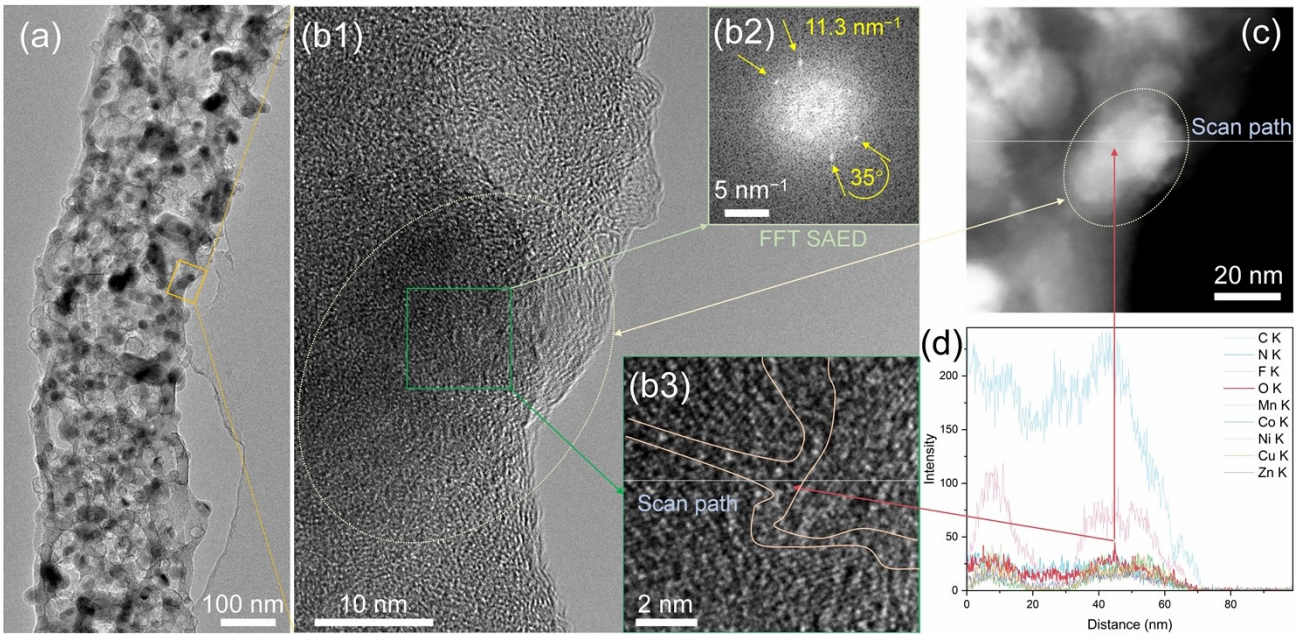

Fig. S15. The HR-TEM images of (MnNiCuCoZn)F_2-PCNFs after 20000 s OER process. **(a)** TEM image, **(b1)** HR-TEM image, **(b2)** the fast Fourier transform (FFT) selected area electron diffraction (SAED) image, **(b3)** corresponding selected area HR-TEM images, **(c)** high angle annular dark field (HAADF) image and **(d)** corresponding linear scanning of EDS.

Table S3. The performance comparison of similar works.

Catalysts	$\Delta E(E_{j=10}-E_{1/2})$ [V]	Peak power density [mW cm^{-2}]	REF
Cu-Co-Mn-Ni-Fe	0.92	165	[8]
FeCoNiMoW	0.75	116.9	[9]
FeNiCrCoMn@CNTs	0.7	128.6	[10]
PtFeCoNiMn	0.724	192.16	[11]
CrMnFeCoNi	0.715	116.5	[12]
CoFeNi@N-PCF	0.7	203	[13]
Fe-Co-Cr@NC	0.71	121.6	[14]
Co/Zn/Mn@NC	0.73	163	[15]
(MnNiCuCoZn)F_2-PCNFs	**0.688**	**206**	**This work**

References

[1] J. Yeh, Alloy design strategies and future trends in high-entropy alloys, Journal of the Minerals Metals and Materials Society 65(2013) (12) 1759-1771. https://doi.org/10.1007/s11837-013-0761-6.

[2] B. Fultz, Vibrational thermodynamics of materials, Prog. Mater Sci. 55(2010) (4) 247-352. https://doi.org/10.1016/j.pmatsci.2009.05.002.

[3] C.M. Rost, E. Sachet, T. Borman, A. Moballegh, E.C. Dickey, D. Hou, J.L. Jones, S. Curtarolo, J.P. Maria, Entropy-stabilized oxides, Nat. Commun. 6(2015) 8485. https://doi.org/10.1038/ncomms9485.

[4] A. Sarkar, L. Velasco, D. Wang, Q. Wang, G. Talasila, L. de Biasi, C. Kubel, T. Brezesinski, S.S. Bhattacharya, H. Hahn, B. Breitung, High entropy oxides for reversible energy storage, Nat. Commun. 9(2018) (1) 3400. https://doi.org/10.1038/s41467-018-05774-5.

[5] Z. Zhu, L. Luo, Y. He, M. Mushtaq, J. Li, H. Yang, Z. Khanam, J. Qu, Z. Wang, M.S. Balogun, High-Performance Alkaline Freshwater and Seawater Hydrogen Catalysis by Sword-Head Structured Mo2N-Ni3Mo3N Tunable Interstitial Compound Electrocatalysts, Adv. Funct. Mater. (2023). https://doi.org/10.1002/adfm.202306061.

[6] T. Xiong, Z. Zhu, Y. He, M.S. Balogun, Y. Huang, Phase Evolution on the Hydrogen Adsorption Kinetics of NiFe-Based Heterogeneous Catalysts for Efficient Water Electrolysis, Small Methods (2023) e2201472. https://doi.org/10.1002/smtd.202201472.

[7] J.A. Dean, N.A. Lange, Lange's handbook of chemistry, McGraw-Hill, inc.1998.

[8] C. Madan, S.R. Jha, N.K. Katiyar, A. Singh, R. Mitra, C.S. Tiwary, K. Biswas, A. Halder, Understanding the evolution of catalytically active multi-metal sites in a bifunctional high-entropy alloy electrocatalyst for zinc–air battery application, Energy Advances 2(2023) (12) 2055-2068. https://doi.org/10.1039/d3ya00356f.

[9] R. He, L. Yang, Y. Zhang, D. Jiang, S. Lee, S. Horta, Z. Liang, X. Lu, A. Ostovari Moghaddam, J. Li, M. Ibanez, Y. Xu, Y. Zhou, A. Cabot, A 3d-4d-5d High Entropy Alloy as a Bifunctional Oxygen Catalyst for Robust Aqueous Zinc-Air Batteries, Adv. Mater. (2023) e2303719. https://doi.org/10.1002/adma.202303719.

[10] X. Cao, Y. Gao, Z. Wang, H. Zeng, Y. Song, S. Tang, L. Luo, S. Gong, FeNiCrCoMn High-Entropy Alloy Nanoparticles Loaded on Carbon Nanotubes as Bifunctional Oxygen Catalysts for Rechargeable Zinc-Air Batteries, ACS Appl Mater Interfaces 15(2023) (27) 32365-32375. https://doi.org/10.1021/acsami.3c04120.

[11] M. Xie, X. Xiao, D. Wu, C. Zhen, C. Wu, W. Wang, H. Nian, F. Li, M.D. Gu, Q. Xu, MOF-mediated synthesis of novel PtFeCoNiMn high-entropy nanoalloy as bifunctional oxygen electrocatalysts for zinc-air battery, Nano Research (2024) https://doi.org/10.1007/s12274-024-6526-4. https://doi.org/10.1007/s12274-024-6526-4.

[12] R. He, L. Yang, Y. Zhang, X. Wang, S. Lee, T. Zhang, L. Li, Z. Liang, J. Chen, J. Li, A. Ostovari Moghaddam, J. Llorca, M. Ibáñez, J. Arbiol, Y. Xu, A. Cabot, A CrMnFeCoNi high entropy alloy boosting oxygen evolution/reduction reactions and zinc-air battery performance, Energy Storage Mater. 58(2023) 287-298. https://doi.org/10.1016/j.ensm.2023.03.022.

[13] M. Li, L. Zong, J. Zhao, K. Fan, F. Song, Q. Zhang, Z. Wang, L. Wang, The millisecond fabrication of medium-entropy alloy as a high-performance bifunctional electrocatalyst for ultralong-term rechargeable zinc–air batteries, J. Alloys Compd. 976(2024) 173183. https://doi.org/10.1016/j.jallcom.2023.173183.

[14] R. Kumar, S. Kumar, S.G. Chandrappa, N. Goyal, A. Yadav, N. Ravishankar, A.S. Prakash, B. Sahoo, Nitrogen-doped carbon nanostructures embedded with Fe-Co-Cr alloy based nanoparticles as robust electrocatalysts for Zn-air batteries, J. Alloys Compd. 984(2024) 173862. https://doi.org/10.1016/j.jallcom.2024.173862.

[15] S. Chen, H. Ren, Y. Qiu, C. Luo, Q. Zhao, W. Yang, Engineering bifunctional electrocatalysts for rechargeable Zn-Air battery by confining Co–Zn–Mn in flower-structured carbon, J. Power Sources 573(2023) 233116. https://doi.org/10.1016/j.jpowsour.2023.233116.